Available online at www.sciencedirect.com
ScienceDirect
Trans. Nonferrous Met. Soc. China 33(2023) 128−140

Transactions of Nonferrous Metals Society of China
www.tnmsc.cn

Cyclic oxidation behavior of Nb/Mn/Si alloying beta−gamma TiAl alloys

Peng-xiang ZHAO[1,2], Xiao-bing LI[2,3], Wei-wei XING[2,4], Bo CHEN[2,4], Ying-che MA[2,4], Kui LIU[2,4]

1. School of Materials Science and Engineering, University of Science and Technology of China, Hefei 230026, China;
2. Shi-changxu Innovation Center for Advanced Materials, Institute of Metal Research,
Chinese Academy of Sciences, Shenyang 110016, China;
3. Jihua Laboratory, Foshan 528200, China;
4. CAS Key Laboratory of Nuclear Materials and Safety Assessment (NMSA),
Institute of Metal Research, Chinese Academy of Sciences, Shenyang 110014, China

Received 18 October 2021; accepted 5 April 2022

Abstract: Cyclic oxidation behavior at 750−850 °C was investigated for Ti42Al1.5Mn3Nb0.1B and Ti42Al1.5Mn-3Nb0.1B0.2C0.2Si alloy by using scanning electron microscopy, electron probe microanalysis, electron backscatter diffraction and X-ray diffraction analysis. The kinetic curves for both alloys roughly follow a parabolic law, with the reduced oxidation rate constant compared to that of Ti42Al5Mn1W alloy at 800 °C. Well-protected oxide films are generated on both alloys at all experimental temperatures, without cracking or spalling of the oxide layer. The addition of Nb inhibits the growth of TiO_2 and promotes the selective oxidation of Al to form a dense and protective Al_2O_3 layer. What is more, the addition of trace Si further promotes the oxidation resistance of the alloy, prompting the alloy to generate a denser alumina layer, which further inhibits the internal diffusion of O and reduces the oxidation mass gain, and this effect is more significant at higher temperatures.

Key words: β−γ TiAl; cyclic oxidation; microstructure; Mn; Nb; Si; alloying

---

1 Introduction

Intermetallic titanium aluminide alloys represent a novel class of innovative structural materials for applications up to 800 °C with attractive properties of high specific yield strength and stiffness, as well as superior creep resistance up to high temperatures [1−3]. In contrast to other high temperature materials, titanium aluminides stand out with the unique combination of low density (3.9−4.2 g/cm^3) and excellent properties, which ideally satisfies the requirements for advanced propulsion systems of aircraft and automobile engine parts, making it a lightweight alternative to conventional Ni-based superalloys [4,5]. However, the poor formability and inadequate oxidation resistance above 800 °C hinder the extensive application of TiAl-based alloys.

In recent years, β-solidifying γ-TiAl alloys based on Ti−(42−44)Al (at.%) have drawn the attention of researchers worldwide due to their excellent formability above 1100 °C [6]. Conventional γ-based TiAl alloys solidifying peritectically via the hexagonal α-phase exhibit anisotropic microstructures as well as significant texture and segregation, while β-solidifying TiAl alloys via body-centered cubic β-phase exhibit isotropic equiaxed as well as texture-free microstructure with modest micro-segregation [7]. A representative

---

Corresponding author: Xiao-bing LI, Tel: +86-15088000846, E-mail: lixb@jihualab.ac.cn;
Kui LIU, Tel: +86-13609875903, E-mail: kliu@imr.ac.cn

DOI: 10.1016/S1003-6326(22)66095-3

example is the Ti42Al5Mn alloy developed by TETSUI et al in 2002 [8], which exhibits excellent hot-deformation behavior that allows low-cost forging under the conventional conditions [9]. However, due to the relatively low Al content, together with the addition of Mn, which is detrimental to oxidation resistance, the high-temperature oxidation performance of Ti42Al5Mn alloy is not ideal [10].

Various methods have been made to improve the oxidation resistance of TiAl alloys, among which alloying is one of the most basic and extensive approaches [10−15]. According to the studies [12,16,17], adding doping elements having higher valence than that of Ti can extensively improve the oxidation resistance of TiAl alloys. Rutile TiO_2 is a non-stoichiometric compound, and by the addition of doping elements such as Nb, W, and Ta, the defect concentration in the oxide can be reduced to maintain electro-neutrality, thus suppressing its formation and growth. Additionally, other elements like Mo are found to be beneficial to the oxidation resistance via enhancing the diffusivity of Al to the surface and promoting the formation of Al_2O_3 [18,19].

In order to design a new alloy that can withstand higher service temperatures, on the basis of Ti42Al5Mn, some compositional adjustments were made. To enhance the oxidation resistance and high-temperature strength of the alloy [3], as well as to prevent possible Laves phase formation [20], Mn was partially substituted with Nb. Boron is beneficial to heat treatments conducted at high temperatures by forming stable borides, which can retard grain coarsening by pinning the grain boundaries [21]. Therefore, for further grain refinement and grain size control, 0.1 at.% B was added. Small additions of C and Si have been found to have a remarkable improvement in the high-temperature strength and creep properties of the alloy due to the solid solution hardening mechanism [22,23] or precipitation strengthening effect of carbide and silicide precipitates [24,25]. What's more, it has been found that adding Nb and Si simultaneously in the coating can significantly improve its high-temperature oxidation resistance, and the synergistic effect of both is significantly preferable to that when being added alone [26]. As a result, 0.2 at.% C and Si were added to improve the mechanical properties of the alloy and to study their effect on oxidation resistance. In light of the reasons above, two new alloys, Ti42Al1.5Mn3Nb-0.1B and Ti42Al1.5Mn3Nb0.1B0.2C0.2Si, were derived from Ti42Al5Mn. Cyclic oxidation tests were conducted for both alloys at 750, 800, and 850 °C for 100 h.

2 Experimental

The as-cast β-stabilized TiAl alloys used in this work, Ti42Al1.5Mn3Nb0.1B and Ti42Al-1.5Mn3Nb0.1B0.2C0.2Si (hereinafter referred to as 0C0Si and 0.2C0.2Si alloys, respectively), were prepared by one-step vacuum induction melting (VIM) using titanium sponge (99.9 wt.%), pure aluminum (99.9 wt.%), niobium (99.95 wt.%), and purified manganese (99 wt.%). The measured chemical composition is presented in Table 1. For oxidation tests, specimens with the dimension of 10 mm × 10 mm × 5 mm were cut from the ingot by electrode discharge machine. The surfaces of the specimens were then ground with SiC papers to 1200 grit, ultrasonically cleaned with alcohol and acetone for 20 min, and finally dried in air.

Table 1 Chemical composition of alloys used in this work (at.%)

Alloy	Ti	Al	Mn	Nb	B	C	Si
0C0Si	Bal.	41.53	1.56	2.92	0.09	−	−
0.2C0.2Si	Bal.	42.31	1.63	3.00	0.09	0.185	0.127

Cyclic oxidation tests were conducted at 750, 800, and 850 °C in a KSL−1200X muffle furnace. Each cycle consisted of an oxidation time of 60 min and a cooling time of 40 min. During oxidation, each specimen was put into a corundum crucible with cover. Any spallation of the oxide scale was retained in the crucible. Mass changes of the specimens along with the crucibles were measured every 10 cycles using a XS105 Dual Range electronic balance (0.1 mg precision). After each measurement, the specimen with the crucible was put into the furnace to heat again. Two samples were tested in identical conditions to verify the reproducibility of the data.

Microstructure morphologies of the two alloys were investigated by using electron probe micro-analyzer in back scattering model (EPMA-BSE) and electron backscatter diffraction (EBSD). The surface and cross-sectional microstructures of samples after oxidation were examined by means of scanning electron microscopy (SEM) equipped with energy dispersive spectroscopy (EDS). Phase constitution of the oxide scales was identified by X-ray diffraction analysis (XRD) with Cu K_α radiation. The specimens were scanned in a 2θ range of 20°−90° with a speed of 8 (°)/min. The elemental mapping of the samples after oxidation was determined by electron probe microanalysis (EPMA, JXA−8530F).

3 Results

3.1 Microstructure of as-cast alloys

The initial microstructures of 0C0Si and 0.2C0.2Si alloys are shown in Fig. 1. As can be observed from the EBSD band contrast and grain orientation maps, both alloys exhibit a similar nearly lamellar (NL) microstructure in the as-cast state with no significant difference in grain size and orientation. The diameter of the lamellar ($\alpha_2+\gamma$)-colonies are well below 50 μm which is much smaller than that of Ti42Al5Mn alloy [27]. Due to the high cooling rate, the lamellar spacing is too small to be resolved at the used magnification. SEM micrographs of both alloys also show borides with either sharp, needle-like, or rather curved and ribbon-like shapes. These borides precipitated before the $\beta\rightarrow\alpha$ reaction, inoculated α nucleation, and contributed to grain refinement [28]. A small amount of black γ phase and white β_0 phase can be observed around the lamellar clusters, due to the fact that Nb and Mn, as β-stabilizing elements, promote the retention of β_0-phase in the alloy. The presence of the β_0 phase distributed around the lamellar colonies inhibits the growth of the original α_2 clusters ($\alpha\rightarrow\alpha_2+\gamma$), thus controlling the size of the lamellar clusters, and plays a role in grain refinement [29]. All these factors above contribute to the more refined grains of 0C0Si and 0.2C0.2Si alloys.

3.2 Oxidation kinetics

Figure 2(a) shows the oxidation mass gain curves of 0C0Si and 0.2C0.2Si alloys after 100 h cyclic oxidation at 750, 800, and 850 °C. It can be seen that the oxidation mass gain of both alloys increases with increasing temperature, and the mass gain of 0.2C0.2Si alloy is less than that of 0C0Si alloy at all tested temperatures, with the trend becoming more pronounced at higher temperatures.

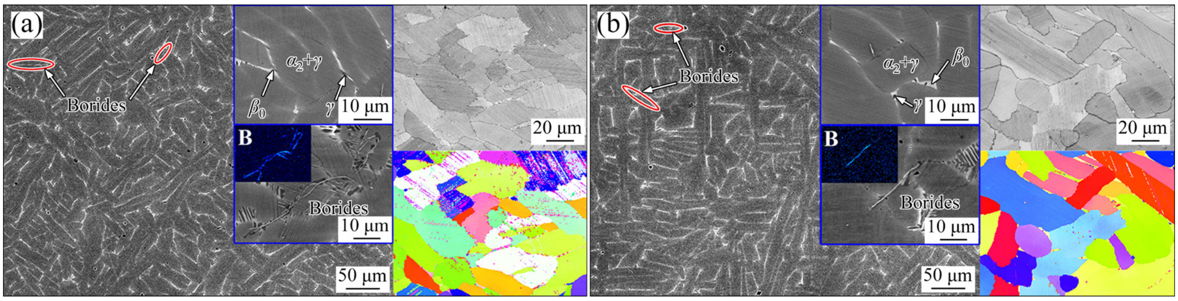

Fig. 1 Initial microstructures of 0C0Si alloy (a) and 0.2C0.2Si alloy (b)

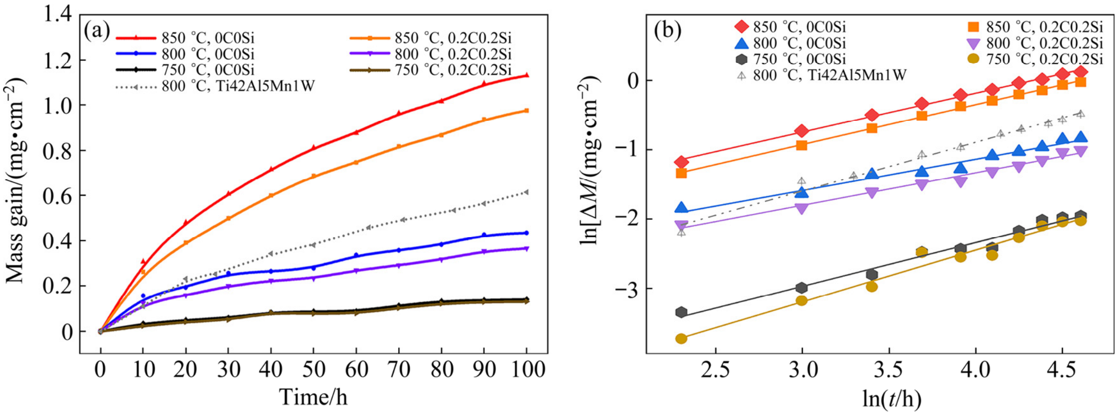

Fig. 2 Variation of specific mass gain versus time at different temperatures (a) and their fitting results (b)

As the knowledge of overall oxidation kinetics is crucial in studying the high-temperature oxidation behavior of the alloys, the relationship between oxidation mass gain and oxidation time is fitted with Eq. (1) [30]:

$$\Delta M^{n}=k_{\mathrm{p}}t \tag{1}$$

where ΔM represents mass gain per unit area (mg/cm^2), n is the power exponent which represents the value of oxidation reaction index, k_{p} is the oxidation reaction rate constant (mg^n/(cm^{2n}·h)) and t is the oxidation time (h). Taking ln−ln plot of the mass gain versus time, we can obtain:

$$\ln\Delta M = 1/n\ln t + 1/n\ln k_{\mathrm{p}} \tag{2}$$

Figure 2(b) shows the results of the regression linear fitting on the data points of the $\ln \Delta M - \ln t$ curves. The values of n and k_{p} can be calculated by Origin software based on Eq. (2), and the results are listed in Table 2.

Table 2 Oxidation kinetic equation parameters of alloys after cyclic oxidation at 750−850 °C

Temperature/°C	Alloy	n	k_{p}/(mg^n·cm^{-2n}·h^{-1})
750	0C0Si	1.62	0.41×10^{-3}
	0.2C0.2Si	1.37	0.64×10^{-3}
800	0C0Si	2.27	1.39×10^{-3}
	0.2C0.2Si	2.17	1.02×10^{-3}
	Ti42Al5Mn1W [10]	1.42	5.15×10^{-3}
850	0C0Si	1.82	13.06×10^{-3}
	0.2C0.2Si	1.77	9.80×10^{-3}

The kinetic curve follows a liner law when $n\approx1$ while follows a parabolic law when $n\approx2$ [12]. The former suggests that the mass gain is proportional to time, which usually implies poor oxidation resistance, while the latter indicates that the oxidation process is mainly controlled by ion diffusion, implying a good oxidation resistance of the oxide layer. According to the results in Fig. 2 and Table 2, at 750 °C, the oxidation kinetic curves of 0C0Si alloy and 0.2C0.2Si alloy follow a pseudo-parabolic law, while the curves of both alloys at 800 and 850 °C roughly follow the parabolic law. The fitting results indicate that the oxidation process of the two alloys is diffusion-driven during the cyclic-oxidation experiment at high temperatures. The oxidation reaction rate constants of the two alloys constantly increase with increasing temperature. At 750 °C, the oxidation mass gain of the two alloys is small, and the oxidation reaction rate constants are similar. Compared to 750 °C, the oxidation reaction rate constant for both alloys almost doubles at 800 °C and is increased by order of magnitude at 850 °C. It is known that a smaller oxidation reaction rate constant reflects a better oxidation resistance of the alloy [31]. In the present study, the k_{p} value for 0.2C0.2Si alloy is significantly smaller than that of 0C0Si alloy at 800 and 850 °C, which allows us to conclude that under the oxidation conditions used in this work, 0.2C0.2Si alloy has a better oxidation resistance. These fitting results are also in good agreement with the kinetic curve results. In this regard, it is reasonable to infer that the addition of trace C and Si elements slightly improves the oxidation resistance of the alloy. In addition, cyclic oxidation mass gain of as-cast Ti42Al5Mn1W alloy at 800 °C [10] is also provided for comparison. It can be found that under the same experimental conditions, compared to Ti42Al5Mn1W, the power exponents of 0C0Si and 0.2C0.2Si alloy are larger and the oxidation reaction rate constants are smaller, indicating an improved cyclic oxidation behavior for the new alloys.

3.3 Phase composition

Figure 3 shows XRD patterns of 0C0Si and 0.2C0.2Si alloy after 100 h of cyclic oxidation at 750−850 °C. The oxidation surfaces of two alloys at 750, 800, and 850 °C are mainly composed of TiO_2 and Al_2O_3, the mixture of which can usually be observed during high-temperature oxidation due to their similar growth dynamics [12]. At 750 °C, because of the small oxide scale thickness, strong peaks of γ-TiAl can be observed. With the increase of cyclic oxidation temperature, the peak intensity of TiO_2 and Al_2O_3 becomes stronger. In addition, for both alloys, small peaks of TiN and Ti_2AlN can also be found at all experiment temperatures. The high similarity of phase composition in these two alloys indicates that the addition of trace C and Si does not change the main phase composition of the oxide scale at different temperatures.

3.4 Oxide morphology and composition

3.4.1 Surface morphology

The surface morphologies of 0C0Si and 0.2C0.2Si alloys after cyclic oxidation at 750 °C for 100 h are shown in Fig. 4. As can be seen, a complete oxide layer has been formed on both alloys, with abrasion marks remaining. TiO_2 particles on the outermost layer are small and do not completely cover the outer surface; beneath this layer is a mixed layer consisting of TiO_2 and Al_2O_3 visible from the outer surface. No spallation can be observed, indicating a strong adhesion between the oxide scale and matrix. Figures 5 and 6 show the surface morphologies of the alloys after 100 h cyclic oxidation at 800 and 850 °C, respectively. As can be seen, with the cyclic oxidation temperature increasing to 800 °C, the abrasion marks on the outer surface become less visible. As it shows from the magnified image, TiO_2 particles with crystal structure on the surface become more significant, mixed with irregularly shaped Al_2O_3 particles. After 100 h cyclic oxidation at 850 °C, no traces of abrasion marks can be observed on the surface, the coarsening and growth of TiO_2 particles on the surface become more obvious with the surface of the outermost layer mainly covered by TiO_2, and the proportion of Al_2O_3 decreases significantly. It is worth mentioning that after 100 h cyclic oxidation at 800 and 850 °C, both alloys still suffer no cracking or spalling of the oxide film, which proves their superior high-temperature oxidation property.

3.4.2 Cross-sectional morphology

The cross-sectional morphologies of the oxide layers of 0C0Si and 0.2C0.2Si alloys after 100 h cyclic oxidation at 800 and 850 °C are shown in Figs. 7 and 8, respectively. With the increase of temperature, the average thickness of the oxide scale for 0C0Si and 0.2C0.2Si alloys increases from 3.1 and 2.1 μm to 7.6 and 6.5 μm, respectively. The oxide scale of both alloys shows a similar layered structure, with the order of $TiO_2/Al_2O_3/TiO_2$+minor Al_2O_3 from outside to inside. After cyclic oxidation at 850 °C, a small amount of oxide nodules appear in the oxide layer of 0C0Si alloy. In addition, the oxide layer of both alloys is relatively flat in general and keeps a good bonding with the substrate, without any visible cracking or peeling.

The cross-sectional back-scattering EPMA image and elemental mappings of the two alloys after 100 h cyclic oxidation in air at 750, 800, and

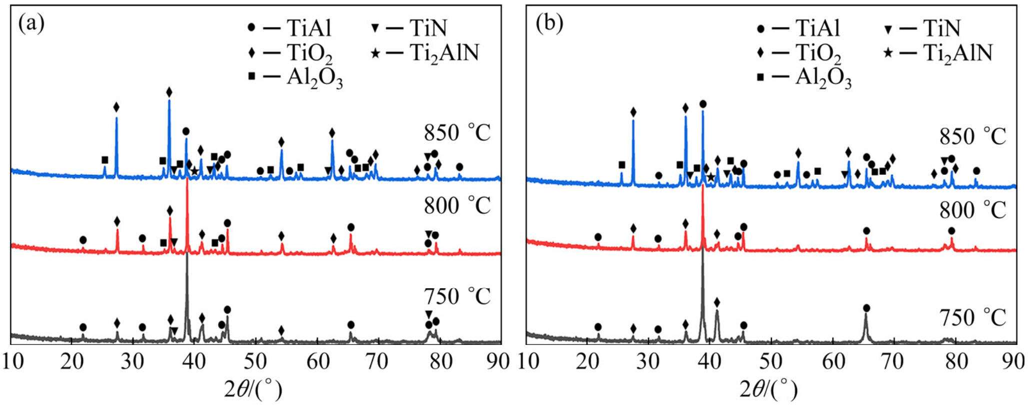

Fig. 3 XRD patterns of 0C0Si (a) and 0.2C0.2Si (b) alloys after cyclic oxidation at 750−850 °C

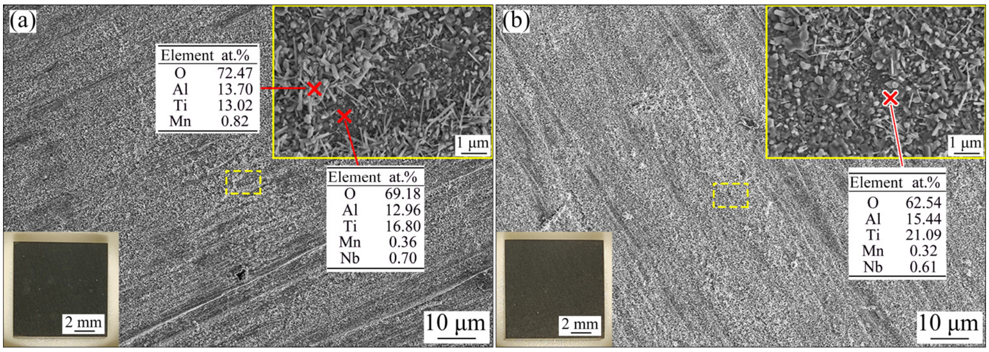

Fig. 4 Surface morphologies of alloys after 100 h cyclic oxidation at 750 °C: (a) 0C0Si; (b) 0.2C0.2Si

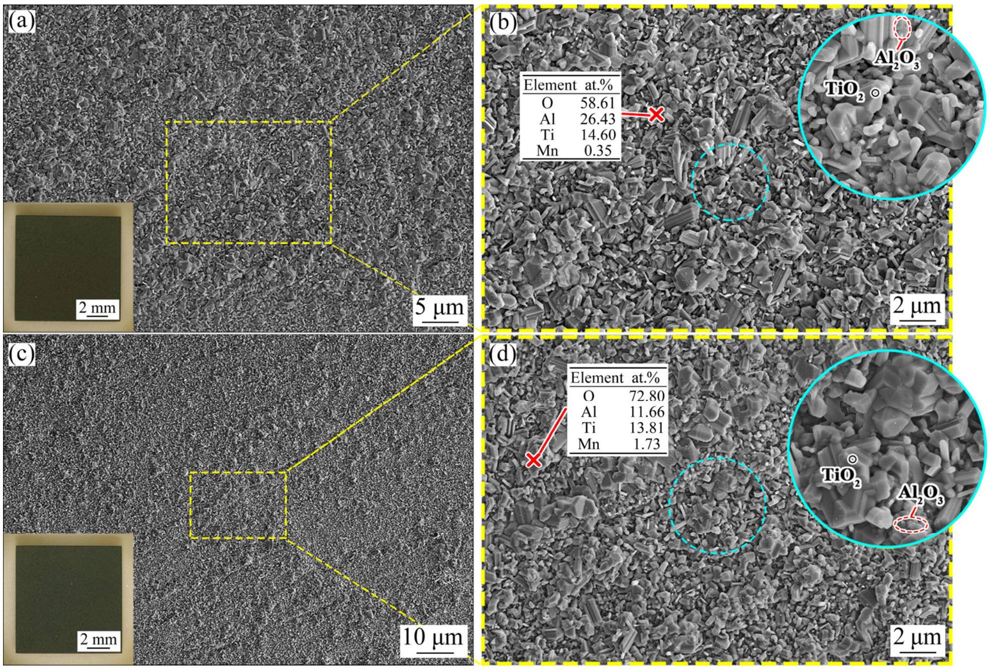

Element	at.%
O	58.61
Al	26.43
Ti	14.60
Mn	0.35

Element	at.%
O	72.80
Al	11.66
Ti	13.81
Mn	1.73

Fig. 5 Surface morphologies of alloys after 100 h cyclic oxidation at 800 °C: (a, b) 0C0Si; (c, d) 0.2C0.2Si

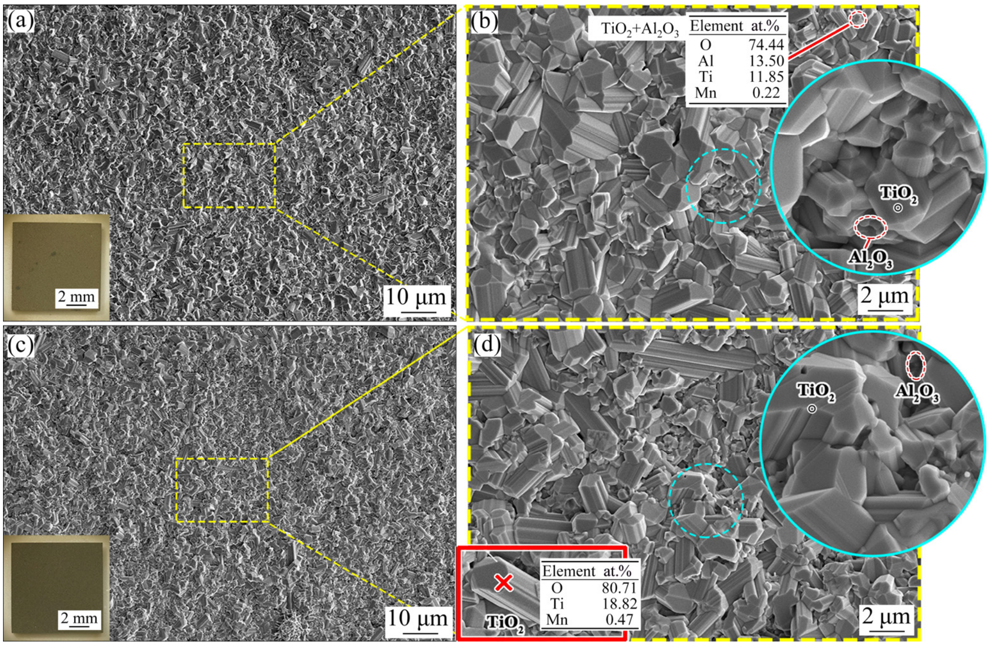

Element	at.%
O	74.44
Al	13.50
Ti	11.85
Mn	0.22

Element	at.%
O	80.71
Ti	18.82
Mn	0.47

Fig. 6 Surface morphologies of alloys after 100 h cyclic oxidation at 850 °C: (a, b) 0C0Si; (c, d) 0.2C0.2Si

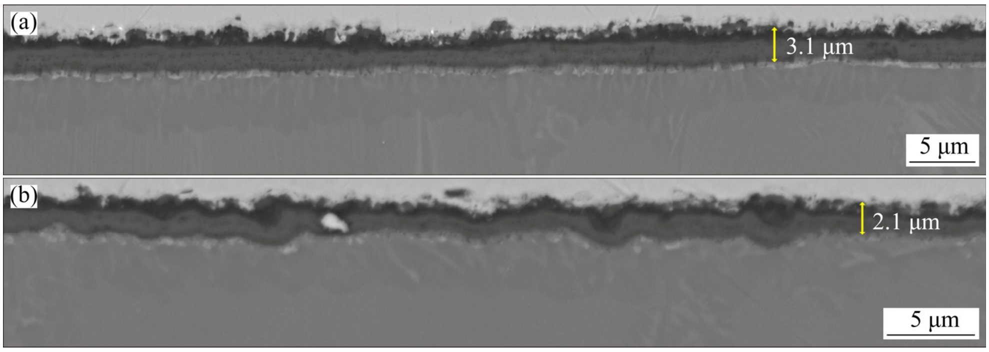

Fig. 7 Cross-sectional morphologies of alloys after oxidation at 800 °C: (a) 0C0Si; (b) 0.2C0.2Si

850 °C are shown in Figs. 9, 10, and 11, respectively. At 750 °C, the oxide scales formed on both alloys share a similar structure; the layered structure can still be distinguished despite the small thickness. Combined with previous SEM results, it can be revealed that the outer surface of the oxide layer is a mixture of Al_2O_3 and TiO_2, and beneath it is a dense Al_2O_3 layer, which shows a dark gray

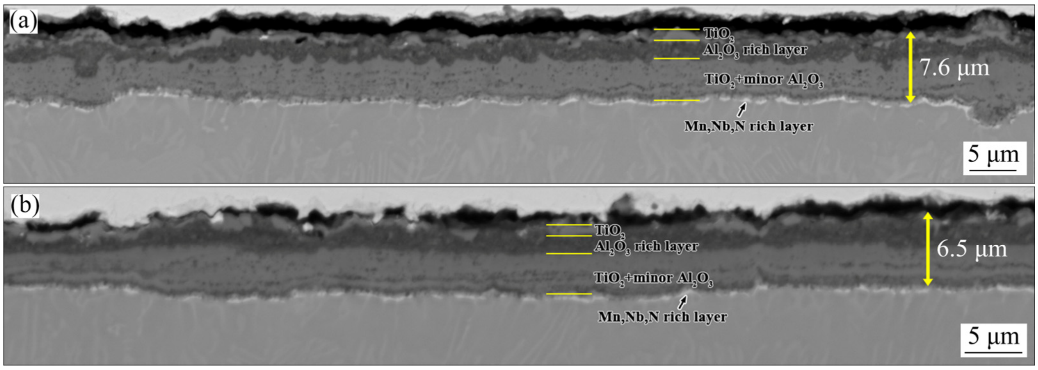

Fig. 8 Cross-sectional morphologies of alloys after oxidation at 850 °C: (a) 0C0Si; (b) 0.2C0.2Si

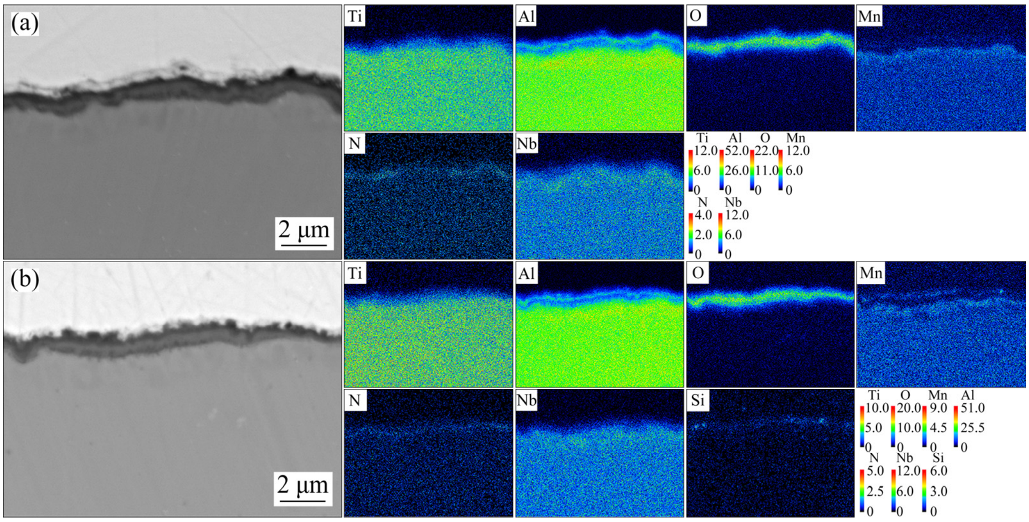

Fig. 9 EPMA back-scattering image and elemental mappings of cross-section of 0C0Si (a) and 0.2C0.2Si (b) alloys after 100 h cyclic oxidation at 750 °C

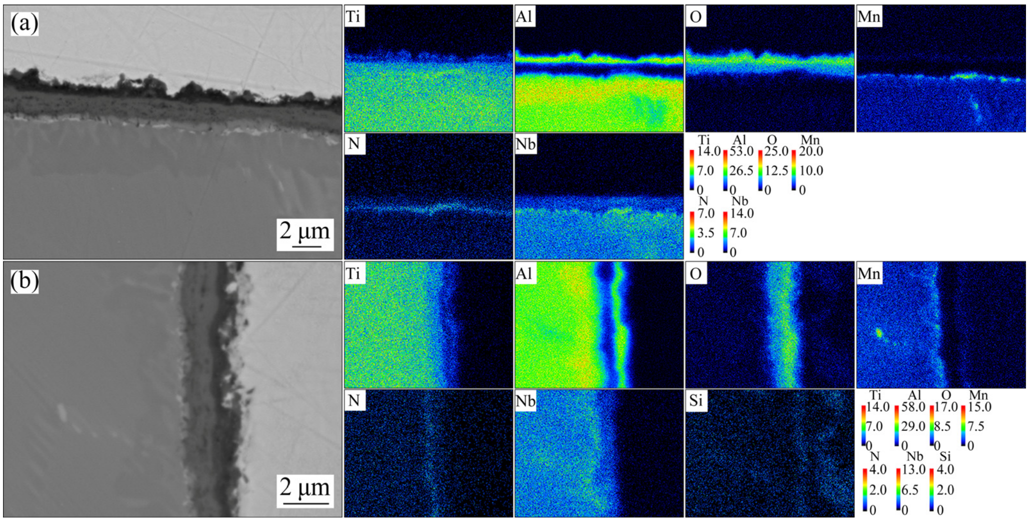

Fig. 10 EPMA back-scattering image and elemental mappings of cross-section of 0C0Si (a) and 0.2C0.2Si (b) alloys after 100 h cyclic oxidation at 800 °C

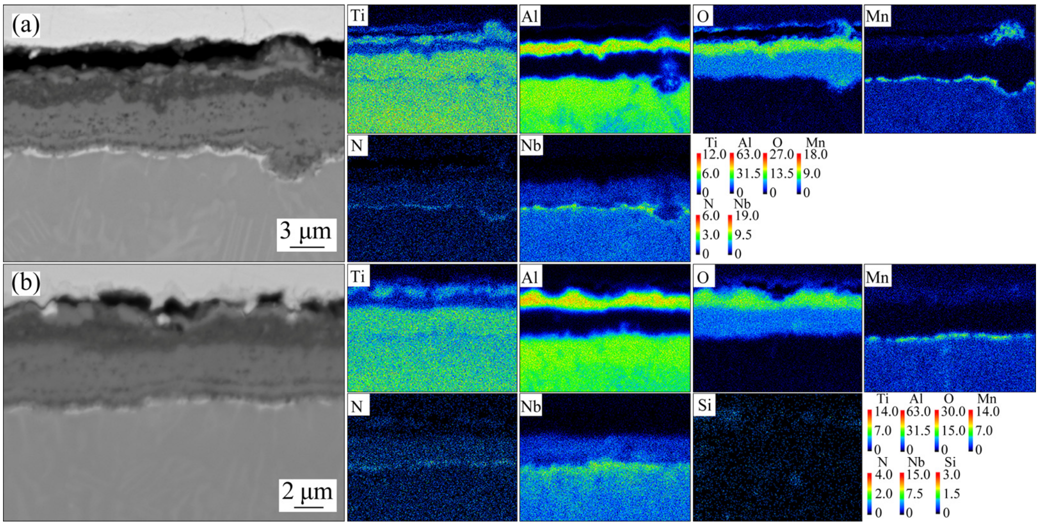

Fig. 11 EPMA back-scattering image and elemental mappings of cross-section of 0C0Si (a) and 0.2C0.2Si (b) alloys after 100 h cyclic oxidation at 850 °C

contrast in the images; the innermost layer is mainly composed of TiO_2, which shows a light gray contrast. In the area of the metallic substrate, the enrichment of N, Nb, and Mn elements can be observed; the former is caused by the internal diffusion of N elements, whereas the enrichment of Nb and Mn is due to the slower diffusion rate of these elements compared to that of Ti and Al during the oxidation process. As a result, they do not diffuse simultaneously with Al and Ti outward but stay in the substrate. A similar phenomenon can be found in some other Nb-, Cr-, and Mo-containing alloys [10,32,33]. As the cyclic oxidation temperature is increased to 800 °C, the thickness of the oxide film increases significantly, with the layered structure becoming more obvious. The outermost layer is a discontinuous TiO_2 layer; beneath it is a dense Al_2O_3 layer, while the innermost layer is still a TiO_2-rich layer. In both alloys, the enrichment of N, Nb, and Mn elements at the metallic substrate between the oxide layer and the matrix becomes more pronounced than that at 750 °C, with a higher degree for 0C0Si alloy than 0.2C0.2Si alloy. This is probably due to the denser and more protective oxide film generated by the 0.2C0.2Si alloy, which better inhibits element diffusion. At the same time, enrichment of Al in the matrix next to the oxide layer is found in the elemental mappings, and the Al-rich layer becomes thicker with the thickening of the oxide layer.

At 850 °C, the oxide scales of 0C0Si and 0.2C0.2Si alloys show some variations after 100 h of cyclic oxidation. The main difference is that in 0C0Si alloy, some oxide nodules are distributed at intervals in the oxide layer, which can be found by the elemental mappings to be oxides of Ti and Mn at the outer part and a mixture of Al_2O_3 and TiO_2 in the substrate side. The rest of the oxide layer of 0C0Si alloy is similar to that of 0.2C0.2Si alloy in terms of composition, where both share the multilayer structure of $TiO_2/Al_2O_3/TiO_2+Al_2O_3$. For the 0.2C0.2Si alloy, no enrichment of C/Si elements is observed in the substrate and oxide layer, probably due to the low addition. The enrichment of Si elements in the elemental mappings in Fig. 10(b) is due to the residue of SiO_2 polishing paste.

4 Discussion

In the present work, the cyclic oxidation properties of two new Mn-containing alloys derived from Ti42Al5Mn were tested at 750, 800, and 850 °C for 100 h. Based on the above experimental results, it can be found that both alloys exhibit excellent high-temperature oxidation resistance at all experiment temperatures, and the cyclic-oxidation resistance at 800 °C is even better than that of Ti42Al5Mn1W alloy. The improved oxidation resistance is mainly attributed to the partial substitution of Mn by Nb in the alloy, which affects ion diffusion and grain refinement by adding B. The addition of trace Si elements may also play a role.

4.1 Influence of Nb and Mn

During the oxidation of TiAl at high temperatures, diffusion in the oxide layer exists mainly in two directions, the external diffusion of metal cations and the internal diffusion of O, N, and other anions [32]. Due to the relatively close thermodynamic Gibbs energy of TiO_2 and Al_2O_3 over a wide temperature range, oxidation of both tends to occur simultaneously [34,35]. Meanwhile, since the diffusion rate of Ti is much higher than that of Al at high temperatures [36,37], the growth rate of TiO_2 is much faster, finally resulting in the layered structure of oxide layers. The inability to form a single dense and protective Al_2O_3 layer leads to the lack of high-temperature oxidation resistance of binary TiAl alloys [16].

Niobium is effective in improving the high-temperature oxidation resistance of TiAl alloys [14,38,39], whose main reaction mechanism can be explained by the doping effect. TiO_2 is the non-metal deficiency n-type oxide, and within it, oxygen vacancies are considered the main defect. It grows mainly by a vacancy mechanism that relies on oxygen diffusion through oxide scales. Therefore, in order to maintain the electroneutrality in the oxide, a doping element with a higher valence than titanium, such as Nb^{5+}, is expected to reduce the oxygen vacancy concentration and thus inhibit the growth of TiO_2. As observed from the EPMA results in Fig. 11, Nb evenly distributed in the inner TiO_2 layer inhibits its growth and gives the Al element sufficient time to oxidize to form Al_2O_3. This is why after cyclic oxidation at 750 and 800 °C, the TiO_2 formed on the outmost layer does not completely cover the alloy surface, and no coarse TiO_2 columnar crystals are observed. In addition, Nb elements are also found to modify the activity of Ti and Al, reducing the critical content of Al elements required for the formation of external dense alumina scales [38]. In the present study, Al content in the alloy (42 at.%) is far below the necessary content required (60−70 at.%) for the formation of a protective aluminum scale in binary TiAl alloys [40] and lower than that of conventional γ-TiAl alloys. However, compared to Ti42Al5Mn, which produced a thick TiO_2/Al_2O_3 mixed layer and suffered severe spallation during the cyclic-oxidation at 800 °C [10], the addition of Nb contributes to forming a continuous and dense Al_2O_3 layer in 0C0Si alloy at all cyclic oxidation temperatures, which hinders the inward diffusion of O during the oxidation process and greatly improves its high-temperature oxidation resistance.

As for Mn, despite its great benefits in grain size and plasticity improvement of the alloys [41], many studies have reported its detrimental effects on high-temperature oxidation resistance [42,43]. Oxidation of Mn was found in some Mn-containing alloys, such as Ti48Al2Mn and Ti48Al2Mn1Mo [30], where the presence of Mn was found in the oxide scale. HAANAPPEL et al [44] found that Mn is generally located in the outer part of the oxide scale and oxide cracks and concluded that the formation of Mn oxide had a detrimental effect on the protectivity of the alumina-rich scale, which was harmful to the oxygen resistance of the alloy. In Ti42Al5Mn alloy, it was also found that during the oxidation process, Mn diffused outward, was oxidized to Mn_2O_3 and doped with TiO_2 at the outmost layer, which would make the oxide scale easy to spall off and damage the high-temperature oxidation resistance of the alloy [10]. However, despite the reduced Mn content in 0C0Si alloy, after 100 h of cyclic oxidation at 850 °C, external diffusion and oxidation of Mn are still found locally at the oxide nodules (as shown in Fig. 11). Nevertheless, as seen from the experimental results, presumably due to the low Mn content in the alloy, the oxide film still maintains good integrity without any peeling. The schematic diagram of the oxide layer of 0C0Si alloy at high temperatures is shown in Fig. 12(a).

4.2 Effect of microstructure

The refined microstructure by adding B and the β-stabilizing elements Nb/Mn in appropriate amounts may also contribute to the improved high-temperature cyclic oxidation resistance of 0C0Si alloy. During cyclic oxidation, thermal and growth stresses in the oxide layer are the leading causes for cracking and spallation. Due to the difference in the coefficient of thermal expansion between the oxide layer and the substrate, large temperature variations that exist during the heating and cooling process during cyclic oxidation will cause thermal stresses, which can easily lead to cracking. Typically, during the cooling process, compressive stresses exist in the oxide layer and

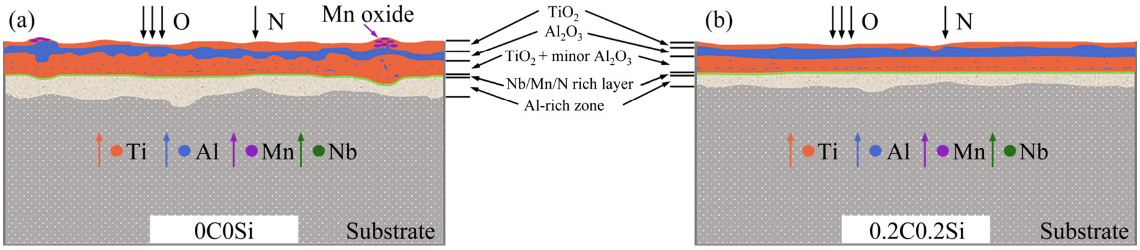

Fig. 12 Schematic diagram of mechanism for 0C0Si (a) and 0.2C0.2Si (b) alloys after cyclic oxidation

tensile stresses in the substrate, which can be released through creep behavior and cracking/ spalling of the oxide layer. TIAN et al [45] found that the resistance to spallation of TiAl alloys with NL structure obtained by heat treatment was significantly higher than that of the alloys containing more β-phases. Compared to Ti42Al5Mn, smaller grain sizes are obtained due to B addition. Mn has a stronger β-stabilizing effect than Nb [46]; with an appropriate partial substitution of Mn by Nb, the residual β_0-phase at room temperature is minimized while ensuring that the alloy is still solidified via β-phase. As a result, NL structures with fine lamellar sizes are obtained in the alloy. The fine lamellar structure can facilitate the release of stresses between the oxide layer and the substrate, thus strengthening the bond between them [47]. This partly explains why 0C0Si alloy does not exhibit any spallation at all cyclic oxidation temperatures in the present study.

4.3 Improvement effect of trace Si

The improved oxidation resistance of 0.2C0.2Si alloy than that of 0C0Si alloy at all experiment temperatures, especially at 850 °C, is mainly attributed to the addition of trace amounts of Si. It was reported that the addition of Si consistently improves the oxidation resistance of TiAl alloys [43,48,49]. Si has a great affinity with Ti and low solubility in the γ phase at both room and elevated temperatures; therefore, the formation of silicide precipitates like Ti_5Si_3 is commonly observed in Si-containing alloys [50]. These silicide precipitates usually locate below the oxide layer in the early stage of oxidation and provide a barrier to oxygen but are then oxidized to form SiO_2 in the scale [49]. Moreover, Si is also reported to increase the diffusion coefficient of Al to promote the formation of a protective Al_2O_3 layer [51,52]. Therefore, in the present study, although no silicide formation was observed below the oxide layer probably due to the low content of Si (0.127 at.%) addition in the alloy, its high affinity with Ti may, in turn, increase the activity of Al and favor the selective oxidation of Al. The synergistic effect of Si and Nb further accelerates the formation of the protective Al_2O_3 layer, resulting in a smaller mass gain for the 0.2C0.2Si alloy. Similar findings have been seen in studies that adding Nb and Si simultaneously in the coating can significantly improve its high-temperature oxidation resistance. Synergistic effect is significantly preferable [26]. The flatter oxide film with a denser and more protective Al-rich oxide layer at high temperatures (850 °C) better inhibits the internal diffusion of O and eliminates the oxide nodules that exist locally in the 0C0Si alloy. In this way, the outward diffusion of Mn is also inhibited, without Mn oxides in the outermost layer, thus reducing the risk of spallation. These factors above finally lead to a further improvement of the high-temperature cyclic oxidation resistance of 0.2C0.2Si alloy. The schematic diagram is shown in Fig. 12(b).

Although an alloy with better oxidation resistance is obtained by the addition of trace Si, in this study, the presence of the Si-rich phase is not detected by SEM−EDS and EPMA due to the low addition content and the limited detection accuracy. Further research needs to be conducted to clarify its mechanism.

5 Conclusions

(1) Cyclic-oxidation at 750, 800, and 850 °C for 100 h was conducted for two new Mn, Nb containing alloys with NL structure and fine lamellar sizes derived from Ti42Al5Mn. Both alloys exhibit improved cyclic-oxidation behavior with a much lower oxidation reaction rate constant than Ti42Al5Mn1W alloy and suffer no spallation

of the oxide scale at all experiment temperatures.

(2) Partial substitution of Mn with Nb significantly reduces the oxidation of Mn and increases the spallation resistance of the alloy. The addition of Nb inhibits the growth of TiO_2 and promotes the selective oxidation of Al to form a dense and protective Al_2O_3 layer during the oxidation process, which effectively inhibits the internal diffusion of O, thereby significantly reducing the oxidation mass gain, and improving the high-temperature oxidation resistance of the alloy.

(3) The fine lamellar structure facilitates the release of thermal and growth stresses in the oxide layer during cyclic-oxidation, strengthening the bond between the oxide scale and the substrate, which partly contributes to the fine spallation resistance of the alloy.

(4) The addition of trace Si elements plays a role in the selective oxidation of Al and further accelerates the formation of the protective Al_2O_3 layer under the synergistic effect with Nb, resulting in a further improvement in high-temperature oxidation resistance of 0.2C0.2Si alloy.

Acknowledgments

This work was supported by the National Natural Science Foundation of China (No. 51971215), and the Natural Science Foundation of Liaoning Province, China (No. 2019-MS-330).

References

[1] CLEMENS H, SMARSLY W. Light-weight intermetallic titanium aluminides-status of research and development [J]. Advanced Materials Research, 2011, 278: 551−556.

[2] YAMAGUCHI M, INUI H, ITO K. High-temperature structural intermetallics [J]. Acta Materialia, 2000, 48: 307−322.

[3] CLEMENS H, MAYER S. Design, processing, microstructure, properties, and applications of advanced intermetallic TiAl alloys [J]. Advanced Engineering Materials, 2013, 15: 191−215.

[4] BEWLAY B P, NAG S, SUZUKI A, WEIMER M J. TiAl alloys in commercial aircraft engines [J]. Materials at High Temperatures, 2016, 33: 549−559.

[5] CLEMENS H, MAYER S. Intermetallic titanium aluminides in aerospace applications-processing, microstructure and properties [J]. Materials at High Temperatures, 2016, 33: 560−570.

[6] KIM Y W, KIM S L. Advances in materials–processes–application technology: Successes, dilemmas, and future [J]. JOM, 2018, 70: 553−560.

[7] CLEMENS H, WALLGRAM W, KREMMER S, GÜTHER V, OTTO A, BARTELS A. Design of novel β-solidifying TiAl alloys with adjustable $\beta/B2$-phase fraction and excellent hot-workability [J]. Advanced Engineering Materials, 2008, 10: 707−713.

[8] TETSUI T, SHINDO K, KOBAYASHI S, TAKEYAMA M. A newly developed hot worked TiAl alloy for blades and structural components [J]. Scripta Materialia, 2002, 47: 399−403.

[9] LI Xiao-bing, XU Hao, XING Wei-wei, CHEN Bo, MA Ying-che, LIU Kui. Phase transformation behavior of a β-solidifying γ-TiAl-based alloy from different phase regions with various cooling methods [J]. Metals, 2018, 8: 731.

[10] ZHAO Peng-xiang, LI Xiao-bing, TANG Hong-jian, MA Ying-che, CHEN Bo, XING Wei-wei, LIU Kui, YU Jian. Improved high-temperature oxidation properties for Mn-containing beta-gamma TiAl with W addition [J]. Oxidation of Metals, 2020, 93: 433−448.

[11] NAVEED M, RENTERIA A F, WEISS S. Role of alloying elements during thermocyclic oxidation of beta/gamma-TiAl alloys at high temperatures [J]. Journal of Alloys and Compounds, 2017, 691: 489−497.

[12] GONG X, CHEN R R, FANG H Z, DING H S, GUO J J, SU Y Q, FU H Z. Synergistic effect of B and Y on the isothermal oxidation behavior of TiAl−Nb−Cr−V alloy [J]. Corrosion Science, 2018, 131: 376−385.

[13] HADI M, BAYAT O, MERATIAN M, SHAFYEI A, EBRAHIMZADEH I. Oxidation properties of a beta-stabilized TiAl alloy modified by rare earth elements [J]. Oxidation of Metals, 2018, 90: 421−434.

[14] LI D X, ZHANG G Y, LU G, WANG J J, LIU C M. Optimizing high-temperature oxidation behaviors of high-Nb-containing TiAl alloys by addition of boron [J]. Corrosion Science, 2020, 177: 108971.

[15] PAN Y, LU X, HUI T L, LIU C C, LIU B W, XU W, ZHANG C, SUN J Z, QU X H, ZHANG J Z. High-temperature oxidation behaviour of TiAl alloys with Co addition [J]. Journal of Materials Science, 2021, 56: 815−827.

[16] NAVEED M, RENTERIA A F, WEIß S. Role of alloying elements during thermocyclic oxidation of β/γ-TiAl alloys at high temperatures [J]. Journal of Alloys and Compounds, 2017, 691: 489−497.

[17] SHIDA Y, ANADA H. The influence of ternary element addition on the oxidation behavior of tial intermetallic compound in high-temperature air [J]. Corrosion Science, 1993, 35: 945−953.

[18] PFLUMM R, DONCHEV A, MAYER S, CLEMENS H, SCHÜTZE M. High-temperature oxidation behavior of multi-phase Mo-containing γ-TiAl-based alloys [J]. Intermetallics, 2014, 53: 45−55.

[19] PÉREZ P, JIMÉNEZ J A, FROMMEYER G, ADEVA P. Oxidation behaviour of a Ti−46Al−1Mo−0.2Si alloy: the effect of Mo addition and alloy microstructure [J]. Materials Science and Engineering A, 2000, 284: 138−147.

[20] TANG Hong-jian, LI Xiao-bing, MA Ying-che, CHEN Bo, XING Wei-wei, ZHAO Peng-xiang, SHU Lei, ZHANG

Meng-shu, LIU Kui. Multistep evolution of β_0 phase during isothermal annealing of Ti−42Al−5Mn alloy: Formation of Laves phase [J]. Intermetallics, 2020, 126: 106932.

[21] HECHT U, WITUSIEWICZ V, DREVERMANN A, ZOLLINGER J. Grain refinement by low boron additions in niobium-rich TiAl-based alloys [J]. Intermetallics, 2008, 16: 969−978.

[22] APPEL F, OEHRING M, WAGNER R. Novel design concepts for gamma-base titanium aluminide alloys [J]. Intermetallics, 2000, 8: 1283−1312.

[23] KIM S W, WANG P, OH M H, WEE D M, KUMAR K S. Mechanical properties of Si- and C-doped directionally solidified TiAl−Nb alloys [J]. Intermetallics, 2004, 12: 499−509.

[24] KARADGE M, GOUMA P I, KIM Y W. Precipitation strengthening in K5-series γ-TiAl alloyed with silicon and carbon [J]. Metallurgical and Materials Transactions A, 2003, 34: 2129−2138.

[25] KIM Y W, KIM S L. Effects of microstructure and C and Si additions on elevated temperature creep and fatigue of gamma TiAl alloys [J]. Intermetallics, 2014, 53: 92−101.

[26] DAI J J, ZHANG H X, SUN C X, LI S Y, CHEN C Z, YANG Y. The effect of Nb and Si on the hot corrosion behaviors of TiAl coatings on a Ti−6Al−4V alloy [J]. Corrosion Science, 2020, 168: 108578.

[27] LI Xiao-bing, TANG Hong-jian, XING Wei-wei, ZHAO Peng-xiang, CHEN Bo, MA Ying-che, LIU Kui. Microstructural stability, phase evolution and mechanical properties of a forged W-modified high-Mn β-γ-TiAl alloy [J]. Intermetallics, 2021, 136: 107230.

[28] HU D W. Role of boron in TiAl alloy development: A review [J]. Rare Metals, 2016, 35: 1−14.

[29] JIN Y G, WANG J N, YANG J, WANG Y. Microstructure refinement of cast TiAl alloys by β solidification [J]. Scripta Materialia, 2004, 51: 113−117.

[30] GARIP Y, OZDEMIR O. A study of the cycle oxidation behavior of the Cr/Mn/Mo alloyed Ti−48Al-based intermetallics prepared by ECAS [J]. Journal of Alloys and Compounds, 2020, 818: 152818.

[31] ZHAO Kun, OUYANG Si-hui, LIU Yong, LIU Bin, LIANG Xiao-peng, LI Hui-zhong, WANG Yu. Isothermal oxidation behavior of TiAl intermetallics with different oxygen contents [J]. Transactions of Nonferrous Metals Society of China, 2019, 29: 526−533.

[32] MAŁECKA J. Transformation and precipitation processes in a metal substrate of oxidized TiAl-based alloys [J]. Oxidation of Metals, 2019, 91: 365−380.

[33] KIM D, SEO D, KIM S W, KIM S, KEUM D, HONG J. Cyclic oxidation behaviors of TiAl−Nb−Si-based alloys [J]. Oxidation of Metals, 2016, 86: 417−430.

[34] RAHMEL A, SCHÜTZE M, QUADAKKERS W J. Fundamentals of TiAl oxidation—A critical review [J]. Materials and Corrosion, 1995, 46: 271−285.

[35] DAS S. The Al−O−Ti (aluminum-oxygen-titanium) system [J]. Journal of Phase Equilibria, 2002, 23: 525−536.

[36] MISHIN Y, HERZIG C. Diffusion in the Ti−Al system [J]. Acta Materialia, 2000, 48: 589−623.

[37] GARIP Y, OZDEMIR O. Comparative study of the oxidation and hot corrosion behaviors of TiAl−Cr intermetallic alloy produced by electric current activated sintering [J]. Journal of Alloys and Compounds, 2019, 780: 364−377.

[38] LIN J P, ZHAO L L, LI G Y, ZHANG L Q, SONG X P, YE F, CHEN G L. Effect of Nb on oxidation behavior of high Nb containing TiAl alloys [J]. Intermetallics, 2011, 19: 131−136.

[39] NEELAM N S, S B, BHATTACHARJEE A, GVS N R, ZAFIR M A. Comparison of the isothermal and cyclic oxidation behavior of Cr and Mo containing γ-TiAlNb alloys [J]. Corrosion Science, 2020, 163: 108300.

[40] SHEN M L, ZHU S L, WANG F H. Formation kinetics of multi-layered interfacial zone between gamma-TiAl and glass-ceramic coatings via interfacial reactions at 1000 °C [J]. Corrosion Science, 2015, 91: 341−351.

[41] HANAMURA T, UEMORI R, TANINO M. Mechanism of plastic deformation of Mn-added TiAl L10-type intermetallic compound [J]. Journal of Materials Research, 1988, 3: 656−664.

[42] KEKARE S A, ASWATH P B. Oxidation of TiAl based intermetallics [J]. Journal of Materials Science, 1997, 32: 2485−2499.

[43] SHIDA Y, ANADA H. The effect of various ternary additives on the oxidation behavior of TiAl in high-temperature air [J]. Oxidation of Metals, 1996, 45: 197−219.

[44] HAANAPPEL V A C, SUNDERKOTTER J D, STROOSNIJDER M F. The isothermal and cyclic high temperature oxidation behaviour of Ti−48Al−2Mn−2Nb compared with Ti−48Al−2Cr−2Nb and Ti−48Al−2Cr [J]. Intermetallics, 1999, 7: 529−541.

[45] TIAN S W, HE A R, LIU J H, ZHANG Y F, YANG Y G, ZHANG Y, JIANG H T. Oxidation resistance of TiAl alloy improved by hot-pack rolling and cyclic heat treatment [J]. Materials Characterization, 2021, 178: 111196.

[46] KAINUMA R, FUJITA Y, MITSUI H, OHNUMA I, ISHIDA K. Phase equilibria among α (hcp), β (bcc) and γ (L10) phases in Ti−Al base ternary alloys [J]. Intermetallics, 2000, 8: 855−867.

[47] LI Z W, GAO W, ZHANG D L, CAI Z H. High temperature oxidation behaviour of a TiAl−Al_2O_3 intermetallic matrix composite [J]. Corrosion Science, 2004, 46: 1997−2007.

[48] KIM B G, KIM G M, KIM C J. Oxidation behavior of TiAl-X (X = Cr, V, Si, Mo or Nb) intermetallics at elevated temperature [J]. Scripta Metallurgica et Materialia, 1995, 33: 1117−1125.

[49] FERGUS J W. Review of the effect of alloy composition on the growth rates of scales formed during oxidation of gamma titanium aluminide alloys [J]. Materials Science and Engineering A, 2002, 338: 108−125.

[50] SUN F S, FROES F H S. Precipitation of Ti_5Si_3 phase in TiAl alloys [J]. Materials Science and Engineering A, 2002, 328: 113−121.

[51] ZHU L H, HU M M, NI W Y, LIU Y X. High temperature oxidation behavior of $Ti_{0.5}Al_{0.5}N$ coating and $Ti_{0.5}Al_{0.4}Si_{0.1}N$ coating [J]. Vacuum, 2012, 86: 1795−1799.

[52] SWADŹBA R, SWADŹBA L, MENDALA B, BAUER P-P, LASKA N, SCHULZ U. Microstructure and cyclic oxidation resistance of Si-aluminide coatings on γ-TiAl at 850 °C [J]. Surface and Coatings Technology, 2020, 403: 126361.

Nb/Mn/Si 合金化的 *β*–*γ* 钛铝合金循环氧化行为

赵鹏翔[1,2]，李小兵[2,3]，邢炜伟[2,4]，陈　波[2,4]，马颖澈[2,4]，刘　奎[2,4]

1. 中国科学技术大学 材料科学与工程学院，合肥 230026；
2. 中国科学院 金属研究所 师昌绪创新材料研究中心，沈阳 110016；
3. 季华实验室，佛山 528200；
4. 中国科学院 金属研究所 核用材料与安全评价重点实验室，沈阳 110014

摘　要：利用扫描电子显微镜、电子探针、电子背散射衍射和 X 射线衍射，研究 Ti42Al1.5Mn3Nb0.1B 合金和 Ti42Al1.5Mn3Nb0.1B0.2C0.2Si 合金在 750~850 ℃下的循环氧化行为。两种合金的氧化增质曲线大致符合抛物线规律，且在 800℃的氧化速率常数较 Ti42Al5Mn1W 合金的降低。在所有的实验温度下，两种合金表面都生成保护性良好的氧化膜，没有开裂或剥落发生。Nb 的添加会抑制 TiO_2 的生长，促进 Al 的选择性氧化，使合金形成致密的 Al_2O_3 层。另外，微量 Si 元素的添加进一步提高合金的抗氧化性，使其生成更为致密的 Al_2O_3 层，在氧化过程中进一步抑制氧的内扩散，降低合金的氧化增质，且其效果在高温下更加明显。

关键词：*β*–*γ* 钛铝合金；循环氧化；显微组织；Mn；Nb；Si；合金化

(Edited by Bing YANG)